CHAPTER- 6

MULTIFUNCTIONAL HER/OER/ORR BEHAVIOR WITH ZnO INTERCALATION IN LSFT

Uma Sharma, Priyanka A. Jha, Pardeep K. Jha, Prabhakar Singh, "Advancements in Bifunctional Catalysts for Unitized Regenerative Fuel Cells: Exploring Polaronic Conduction and Heterostructure Designs", (Accepted in Journal of Physics D: Applied Physics).

CHAPTER 6: Multifunctional HER/OER/ORR behavior with ZnO intercalation in LSFT

6.1 Introduction

In the continuation of the previous chapters, LSFT system was chosen as the bifunctional catalyst in the LF perovksite type material. Recent reports suggests that OER and ORR primarily used in the H_2/O_2 fuel cell as well as in a unitized regenerative fuel cell (URFC). Major challenge behind this to explore those catalysis which are highly active and the corrosive resistant with the multifunctional catalyst properties.

In the present chapter, we have tried to investigate the multifunctional properties of LSFT/ZnO/LSFT system with the help of electrochemical studies. Here, LSFT/ZnO/LSFT formed via pulse laser deposition method, taking LSFT and ZnO as target materials and the LSFT as a substrate material in the experiment. Heterostructures formed with the variation of thickness of approximately 2μm, formed varying the number of laser shots. Since, in the last chapter the interesting and the promising properties observed in the environment-friendly medium called as neutral medium, that is why, this study aimed to explore the LSFT/ZnO/LSFT heterostructure as the multifunctional catalyst. Since, there are two heterostructure formed and LSFT is a mixed-ionic electronic conducting material, that is why we named them as double heterostructure mixed-ionic electronic conducting material (DH-MIEC).

In this chapter, the formation of interfacial polarons and polaronic charge modification due to the incorporation of ZnO in LSFT has been discussed. Also, the effect of these modifications on the reaction mechanism has been investigated in detail in the neutral medium.

Here, these catalysts exhibit higher current densities and greater stability in the OER and ORR mechanism in the neutral medium. The chronopotentiometry stability has also been studied. This stability test is also discussed in detail with the help of XPS and FTIR studies in the chapter.

6.2 Experimental Procedure

6.2.1 Target and base materials Preparation

The samples with composition $La_{0.5}Sr_{0.5}Fe_{0.5}Ti_{0.5}O_3$ (LSFT) have been prepared using the conventional Solid State Reaction (SSR) Method. The high purity precursor used in synthesizing the sample powders were Lanthanum (III) oxide (La_2O_3), Iron (III) oxide (Fe_2O_3), and Strontium carbonate ($SrCO_3$), Titanium (IV) oxide (TiO_2) (all from Alpha Aesar with purity more than 99%). Initially, the pre-defined stoichiometric amount of highly purified dry starting materials were weighed and all oxides were intimately mixed by grinding them finely with a mortar and pestle using acetone as a mixing medium for around 2-3 h for preparing each of the sample powders. Then the sample powder was preheated at 300 ℃ for 4 h in a hot air oven. After preheating, the powder was again ground thoroughly. Further ground sample was subjected to calcination at 1200 ℃ for 2 h with the heating rate at 5 ℃/min in the muffle furnace for the completion of the reaction, phase formation and to get rid of impurities like carbonates etc. Further calcined powder was used for the phase and structure determination by X-Ray Diffraction (XRD) instrument in the 2θ range from 10° to 80° with a step size of 0.02° at a scanning rate of 1° /min with Cu-Kα radiation of wavelength (λ) ~ 1.5405 Å. From the calcined powders, three uniform pellets of each sample were prepared for different types of characterisation. For this calcined powder was mixed with the prepared PVA binder solution by grinding it in a mortar and pestle. The resulting powder was made into circular pellets by

applying pressure for one minute using a hydraulic press. These pellets were sintered at 1300 ℃ for 2 h in the muffle furnace for grain growth with the same heating rate. Thereafter, the crystalline phase of the sintered sample was determined by XRD. Thereafter, platinum was pasted on both the faces of the pellets and cured at 750 ℃ for 20 min in the furnace for further measurements.

6.2.2 Heterostructure Fabrication

For heterostructure formation, Pulsed Laser Deposition (PLD) technique was performed. The target materials LSFT and ZnO were mounted on the target holder. The beam of KrF Excimer laser (248 nm) was targeted on the LSFT and ZnO targets. During ablation, the temperature of the deposition chamber was set to 550 ℃ and the frequency was set to 5 Hz and the energies to 375 mJ. Firstly, the substrate for deposition was LSFT pellet and a layer of ZnO is deposited with the variation of shots as 500, 1000, 1500, and 2000. Then, another layer of LSFT was deposited over LSFT/ZnO heterostructure to form LSFT/ZnO/LSFT heterostructure as described in Fig. 6.1(a).

6.2.3 Characterizations

The phase, structure, space group, atomic positions and occupancies of the components of the material is confirmed by Rietveld refinement of the X-ray diffraction data using FULLPROF software. The structural characterization was performed with Cu-Kα radiation of wavelength (λ) ∽1.5405 Å in 2θ range from 20^o to 80^o at a scanning rate of 1 ^{o}/min. The InfraRed absorbance was recorded in the range 500-4000 cm^{-1}. Also, the UV-Visible absorbance spectra of these thin films were recorded in wavelength region 200-900 nm. The I-V characteristics was studied in dark using Keithley-2450 electrometer. The dc conductivity

was extracted from Jonscher power law fitting of conductivity data studied in the frequency range from 1 Hz to 1 MHz and temperature range from 25 ℃ to 700 ℃. Microstructural analysis of the fractured surface of heterostructures was carried out by using a scanning electron microscope (SEM). X-ray photoelectron spectroscopy (XPS) was studied. The morphology was studied using Atomic Force microscopy (AFM). For the electrochemical studies of the sample, cyclic voltammetry has been performed by Keithley 2450 source meter with a three-electrode electrochemical cell, where Ag/AgCl electrode is used as reference electrode, Pt wire as a counter electrode, LSFT and heterostructures as working electrode directly. 1M Sodium Sulphate (Na_2SO_4), a neutral solution having pH factor 7 was used as electrolyte. The chronopotentiometric stability of the material is tested in neutral medium for more than 24 h. The Nernst equation used to calculated the reference potential is [200]–

$$E_{RHE} = E_{cell} + 0.197 + 0.059pH \quad (6.1)$$

The estimations of highest occupied molecular orbitals (HOMO) and lowest unoccupied molecular orbitals (LUMO) were done with the empirical relations discussed in previous chapters (equation 5.2 and 5.3).

6.3 Results and Discussion

6.3.1 Heterostructure formation and Conductivity

Fig. 6.1(a) illustrates the general sample preparation i.e., intercalation of ZnO between LSFT. A pellet with surface area, A~1 cm^2 and thickness, d ≲ 1 mm of LSFT taken as the substrate on which ZnO layer is deposited by PLD. The thickness of ZnO is varied by the number of laser shots (n×100) with n = 5, 10, 15, 20. These ZnO layers are sandwiched by deposition of LSFT layer with 1000 (i.e., $n = 10$) number of laser shots. In this way, there are four double heterostructure-mix ionic electronic conductors (DH-MIEC) as n = 5, 10, 15, 20 and

compared with parent/uncalated LSFT, termed now as $n = 0$. The thickness of the ZnO layer measured using scanning electron microscopy (SEM) (for instance, n =10 is shown in Fig. 6.1(b)) and observed that the thickness is increasing with $'n'$ i.e. ~ 0.7 µm, 1.9 µm, 2.2 µm, 3.5 µm, for n =5, 10, 15, 20, respectively.

Fig. 6.1(c) shows the X-ray diffraction patterns of DH-MIECs and presence of orthorhombic phase (Pbnm) of LSFT (5.530 (3) Å,7.810 (4) Å, 5.555 (1) Å) and hexagonal phase (P63mc) of ZnO (a = b = 3.2494(1) Å, c = 5.2071(1) Å) is revealed[201]. Figure 6.1(d) depicts the dc conductivity (σ) vs temperature (T) plot in the range of 300K-900K for all DH-MIECs with small ac amplitude of 100 mV.

At 300 K, $\sigma_{n=0} \simeq 9.85 \times 10^{-11}$ S/cm for LSFT ($n = 0$) and relative conductivity with respect to $n = 0$ i.e., $\sigma_n/\sigma_{n=0}$ is ~ 4 times for $n = 10$,15, and 20 (Inset Fig. 6.1d). At 900 K, all DH-MIECs show (~5 decades) increase in conductivity due to thermally activated charge carriers. Interestingly, at 900 K, $\sigma_n/\sigma_{n=0} \sim 4.5$, which is maximum for $n = 10$ while for $n = 15$ it drops to ~3. Further, the dc polarization method is used to elucidate electronic behavior, the current density (j) −electric field (E) curves both in forward and reverse voltage scans are recorded at 300 K and plotted (Fig. 6.1(e)). There is no hysteresis curve obtained thus the response of ionic species are almost constant here, and conductivity is significantly prevailed by electronic species here.

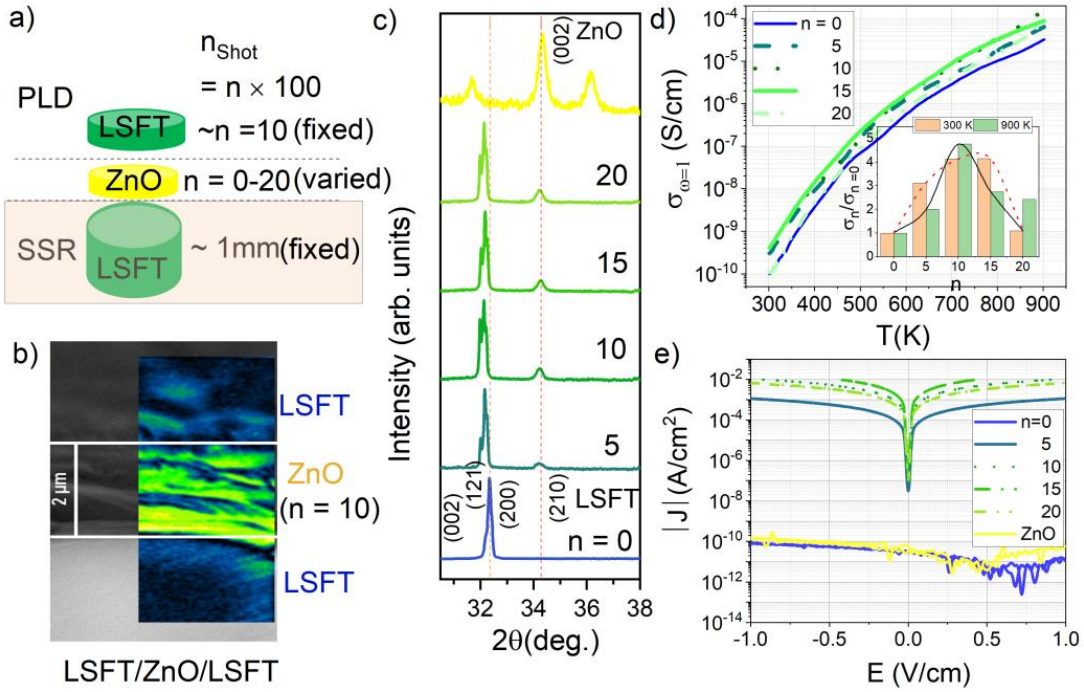

Figure 6.1 **(a)** Heterostructure preparation i.e., intercalation of ZnO between LSFT, **(b)** SEM micrographs for $\boldsymbol{n}$ =10 illustrating the thickness of ZnO layer, **(c)** X-ray diffraction patterns of DH-MIECs and presence of peaks **(d)** Variation dc conductivity with temperature , inset shows the relative conductivity of DH-MIECs with respect to $\boldsymbol{n}$ = **0 (e)** Current density ($\boldsymbol{j}$)vs electric field ($\boldsymbol{E}$) curve.

The important observation is colossal rise in the current density with ZnO intercalation which cannot be accounted for the basis of Drude behavior i.e., an increase in mobility or charge species. At E = 0.1 V/cm, the estimated conductivity for n = 5, 10, 15, 20 are 0.01, 0.11, 0.23, 0.07 S/cm respectively in comparison to 1.1 × 10^{-9} S/cm for n =0.

Fig. 6.2(a) shows the mix ionic electronic behavior for the parent sample along with the DH-MIECs (variation of I/I_o vs. time) using coulometric method. It can be seen that there is a very fast current decay for n = 5 and a very slow decay for n =10. However, for n =10, the transport number is between 0.6 - 0.8 suggesting higher mix ionic electronic as compared to parent and other DH-MIECs.

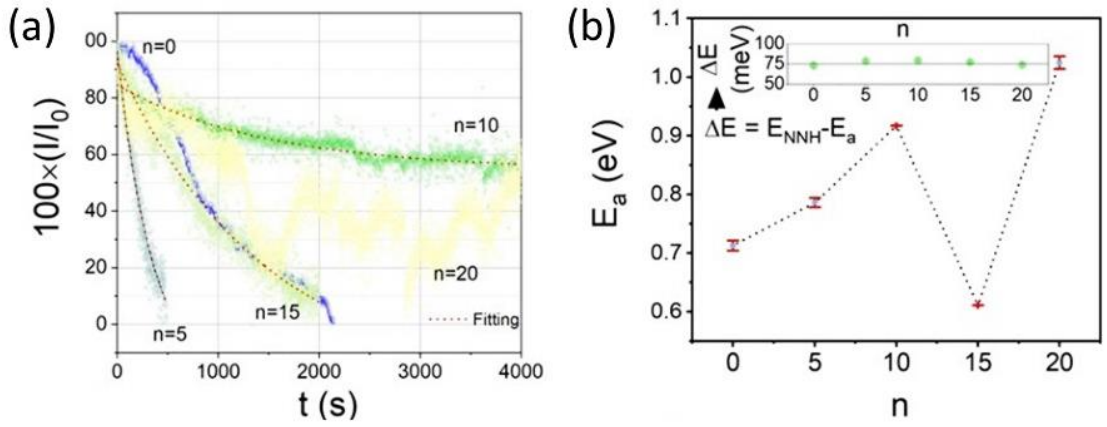

Figure 6.2 (a) Mix ionic electronic behavior for the parent sample along with the DH-MIECs (variation of $\boldsymbol{I/I_o}$ vs. time) using coulometric method **(b)** Activation energy plotted with the $\boldsymbol{n}$ variation, inset shows the difference of activation energies from Arrhenius and nearest neighbor hopping plots of conductivity.

Furthermore, after initial decay, the current decay rate at $n = 15$ is similar to that of LSFT. In order to calculate activation energy, Arrhenius plots of conductivity have been plotted. Inset of Fig. 6.2(b) indicates the difference of activation energies from Arrhenius and nearest neighbor hopping plots of conductivity and is observed to be 75 meV suggesting polaronic conduction which is accordance with the literature[165].

Fig. 6.3(a) shows the variation of transmittance for $n = 10$ and $n = 15$ DH-MIECs. From transmittance plots, Fe-O, La-O, Ti-O, Sr-O and Zn-O have shown their characteristics peaks as marked by arrows in Fig. 6.3(a). There is reduction in transmission in fingerprint region of $n = 15$. The surface topographical image has shown the increase in grain size in $n = 15$ DH-MIEC. As observed from the activation energy plots, E_a is lying between 0.6-1.1 eV suggesting the formation of doubly ionized oxygen vacancies. However, E_a is minimum for $n = 15$ suggesting higher conductivity.

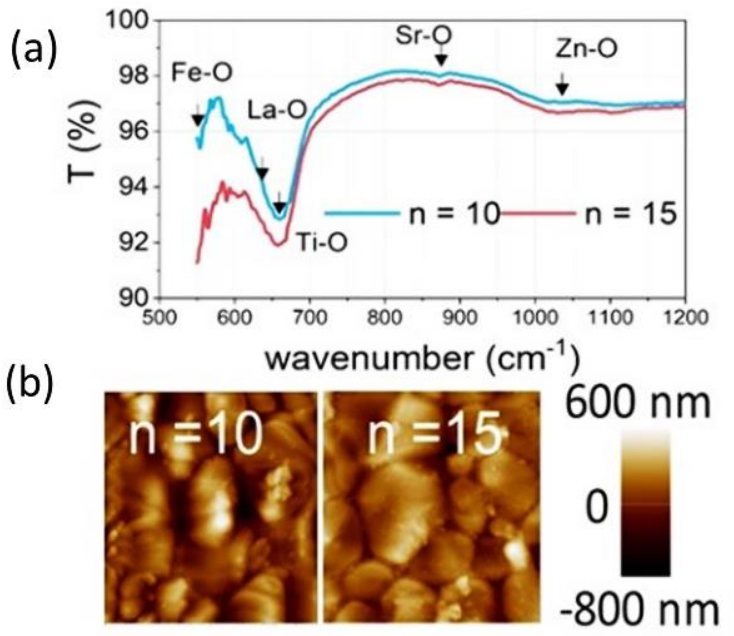

Figure 6.3 **(a)** Variation of transmittance for $\boldsymbol{n} = 10$ and $\boldsymbol{n} = 15$ DH-MIECs, arrows are showing the characteristic peaks corresponding to Fe-O, La-O, Ti-O, Sr-O and Zn-O, **(b)** Surface topographical images from AFM indicating larger grain size and smaller roughness for $\boldsymbol{n}$ =15.

Electronic conductivity occurs via delocalized states in the conduction/valence band or via localized states by a thermally assisted hopping mechanism. The dc polarization method as shown in Fig. 6.1(e) is applied to a mixed ionic electronic conductor placed between two ions blocking and electronically conducting electrodes in which the positively charged oxygen vacancies displace under an applied bias. While the total concentration of oxygen vacancies, conned between the blocking electrodes, is designed to remain fixed, their net redistribution leads to the creation of oxygen vacancy depleted and enriched regions. This results in a redistribution of the electrons, attempting to maintain local charge neutrality, leading to a change in the overall conductivity, dominated by the more mobile electronic species. For an MIEC with a prevailing electronic conductivity, the local depletion in oxygen vacancies leads to an increase in total resistance.

As observed here that electrical conductivity has major role due to oxygen vacancy assisted polaron conduction. Polaron conduction is believed to influence the proton conduction behavior in several ways. Polaronic conduction may affect the activation energy required for proton migration. The presence of polarons can modify the energy landscape for proton hopping, making it easier or more difficult for protons to move between different sites in the lattice. The mix of ionic and electronic conduction can facilitate the establishment of a well-connected catalyst-electrolyte interface. This interface is crucial for promoting effective proton adsorption and facilitating electron transfer to the active sites, ensuring a high catalytic turnover rate. The mix ionic conduction is essential for achieving high-performance air electrodes in various energy conversion and storage systems. It improves oxygen reduction kinetics, reduces polarization losses, enables operation at lower temperatures, enhances tolerance to impurities, and makes the devices compatible with a wider range of fuel options[209].

6.3.2 XPS Analysis

In this section, X-ray photoelectron spectroscopy has been studied. The XPS wide spectra deconvoluted for each element has been analyzed. Here, the deconvoluted spectra corresponding to O has been shown in Fig. 6.4. O 1s peak at ~ 529 eV corresponds to the metal and O bond (Fe-O, Ti-O, Sr-O and La-O) is present in LSFT and n =15 DH-MIEC, while the peak corresponding to metal-OH is present in parent, n =10 and 15 DH-MIECs.

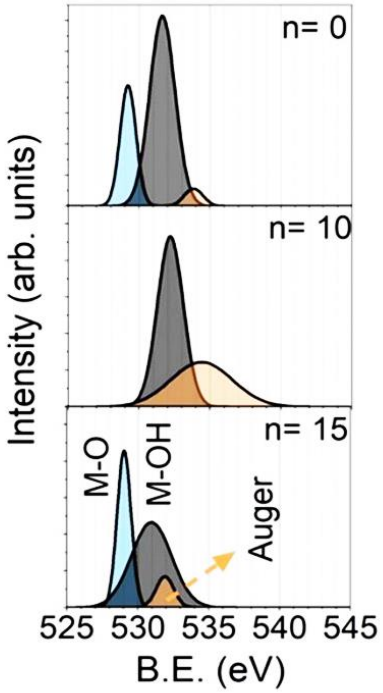

Figure 6.4 Deconvoluted XPS spectra corresponding to O, blue colored peak corresponds to metal-O bond, black colored peak corresponds to metal-OH bond and light orange colored peak corresponds to Auger electrons.

However, the full width at half maximum (FWHM) of metal-OH peak at n =15 is higher than the FWHM at n =10 DH-MIEC. Further, the Auger peak is broad in n =10, as compared to the n =0 and 15. Further a blue shift in the M-OH peak has been observed for n =10 and then a red shift is observed for n =15. This suggests the variation of O oxidation state with the creation of oxygen vacancies compensated by Auger electrons.

6.3.3 Bifunctional Behavior

In order to study the effect of polaron conduction on the multifunctional behavior, electrochemical characterization have been carried out in the neutral medium. The cyclic voltammograms (CV) with the variation of scan rate are shown in Fig. 6.5.

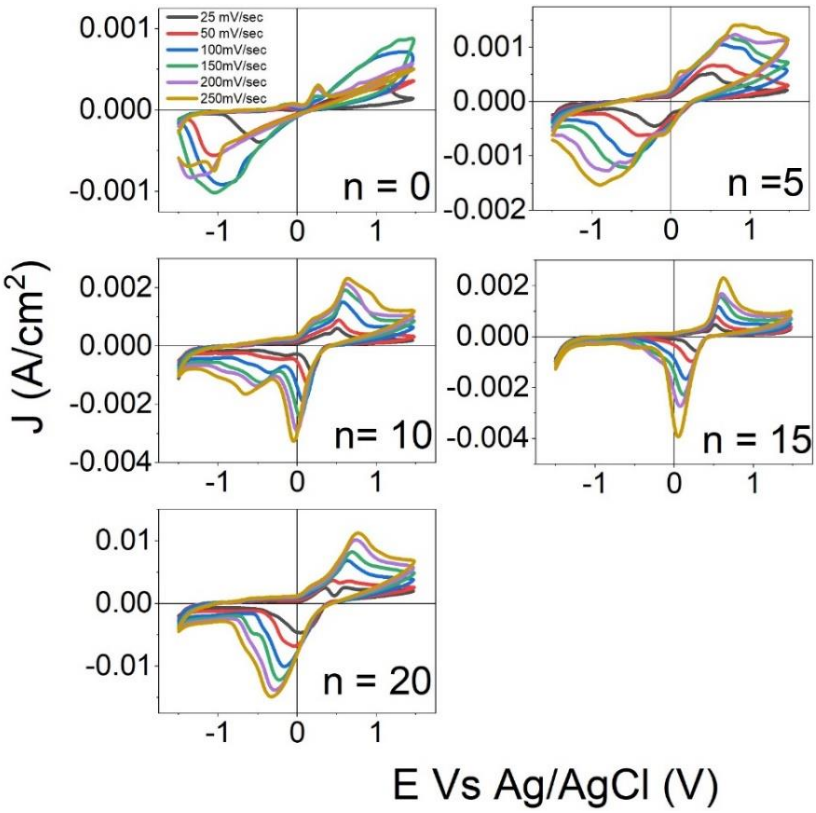

Figure 6.5 Cyclic voltammograms of different DH- MIECs with the variation of scan rate.

The peak current density, j_p is four times higher (4 mA/cm^2) in n =15 as compared to n =0. The catalytic regeneration is observed in n =5 to15 while there is peak splitting along with 'duck' shaped curve at n =5 and 10 DH-MIEC. With the intercalation of ZnO, the metal ligand interaction altered the surface oxygen behavior as revealed in XPS due to polaronic behavior. This interaction will result in alteration in electrochemical behavior as revealed in the CV curves where significant change in oxygen evolution reaction and hydrogen evolution behavior is observed. A mutifunctional beahvior (HER/OER/ORR) is observed for the DH-MIEC (Fig. 6.6(a, b and (c)) while ORR is observed to increase with the increase in thickness. Here, HER and ORR potential shifted to positive potential as shown in Fig. 6.6(a and c).

However, OER potential remains almost in variant with the thickness alteration but significant increase in OER current is observed (Fig 6.6(b)).

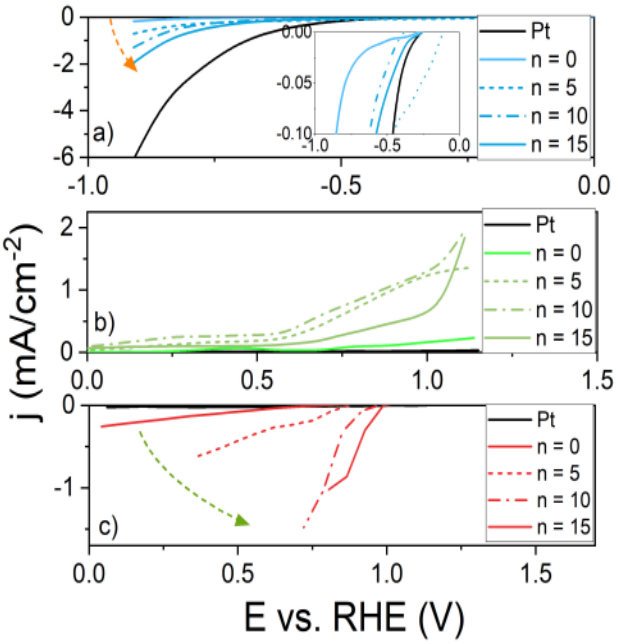

Figure 6.6 Linear sweep voltametric (LSV) curves in **(a)** HER, **(b)** OER and **(c)** ORR regimes and a comparative is prepared with Pt working electrode.

The anodic and cathodic peak potential difference, ΔE_p > 180 mV with the variation of scan rate suggests multiple electron processes for DH-MIECs[158]. In OER regime, the electrochemical reversibility is varied using the linear fitting of the peak current density, $j_p$versus $\upsilon^{1/2}$ via Randles Selvick (RS) equation (equation 3.3)[158]. Linear R-S plots suggest that faradaic currents in OER flow via charge transfer. However, charge transfer occurs via O-diffusion and adsorption. The slope in Fig. 6.7(b), log-log plots of j_p versus scan rate, υ is less than 0.5 showing the failure of the adsorption equation (equation 5.4) and suggesting charge transfer via diffusion.

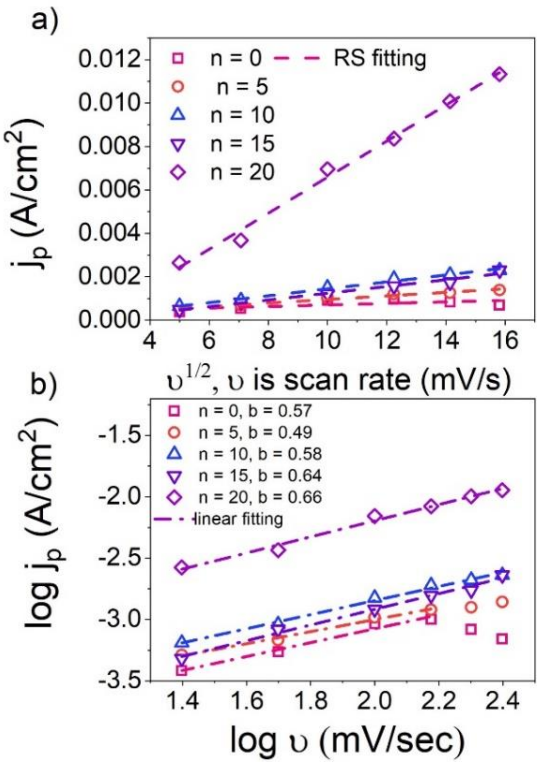

Figure 6.7 **(a)** RS equation plot between the current density and scan rate,υ and **(b)** log-log plot of current density and υ of all DH-MIEC with parent LSFT.

6.3.4 Transient response at interface

The transient current decay time of all DH-MIEC (n =0,5,10,15,20) has been estimated from the exponential decay fitting of chronoamperometric response for shown in Fig. 6.8. The calculated decay time is significantly less in comparison to the parent LSFT (n =0) which suggest that DH-MIECs are more suitable for hole transport due to less transient response.

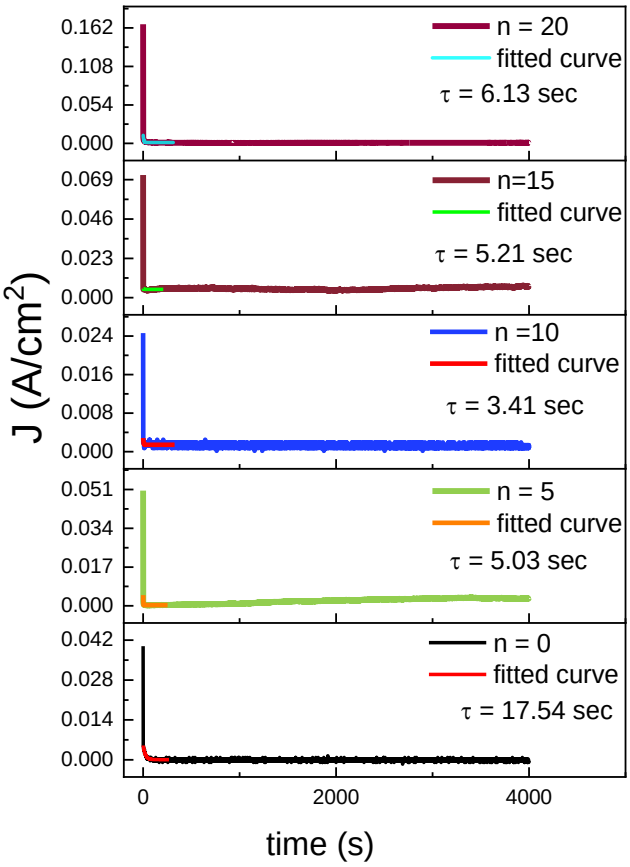

Figure 6.8 Chronoamperometric response of all DH-MIECs with parent LSFT.

Figure 6.9 shows the j vs $t^{-1/2}$ known as Shoup-Szabo relation and number of charge transfer is estimated with help of equation 3.2.

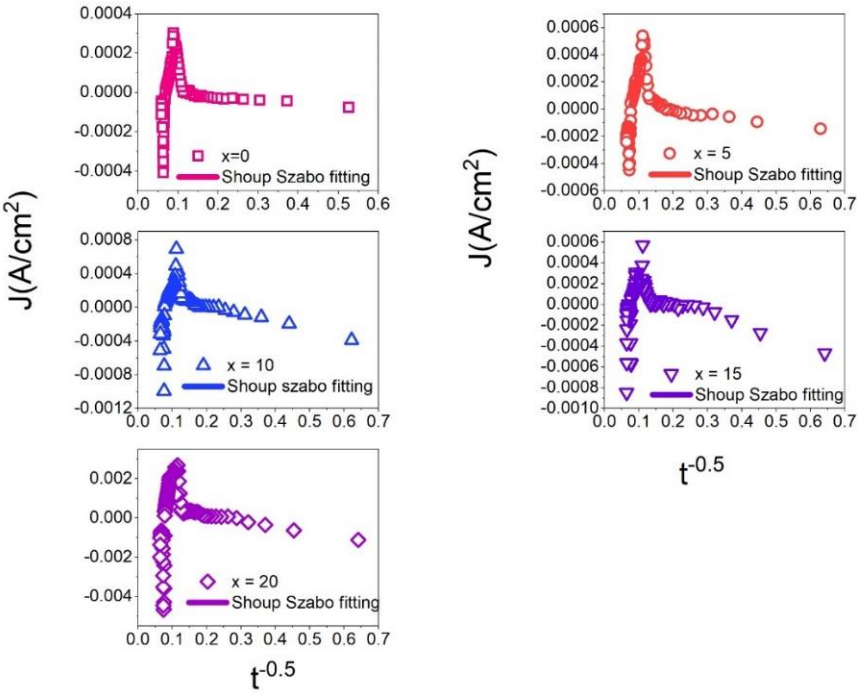

Figure 6.9 Shoup-Szabo fitting of all DH-MIECs with parent LSFT (n=0).

Fig. 6.10 shows the Mott-Schottky analysis [46, 57], it reveals that p-type nature is observed for all DH-MIECs.

As the number of electron transfers is 3 and 4, the mechanism occurs with the formation of water as mentioned below-

$$\frac{1}{4}O_2 + \frac{1}{2}H_2O + e^- \rightleftharpoons OH^- \quad (6.1)$$

$$\frac{1}{2}Fe_2O_3 + 3H^+ + e^- \rightleftharpoons Fe^{2+} + \frac{3}{2}H_2O \quad (6.2)$$

As per relation, e^-, OH^- and O_2 formation is reversible followed by formation of H_2O with an interconvertible state of Fe-ion ($Fe^{2+} \Longleftrightarrow Fe^{3+}$). This water formation leads to the multifunctional behavior[210].

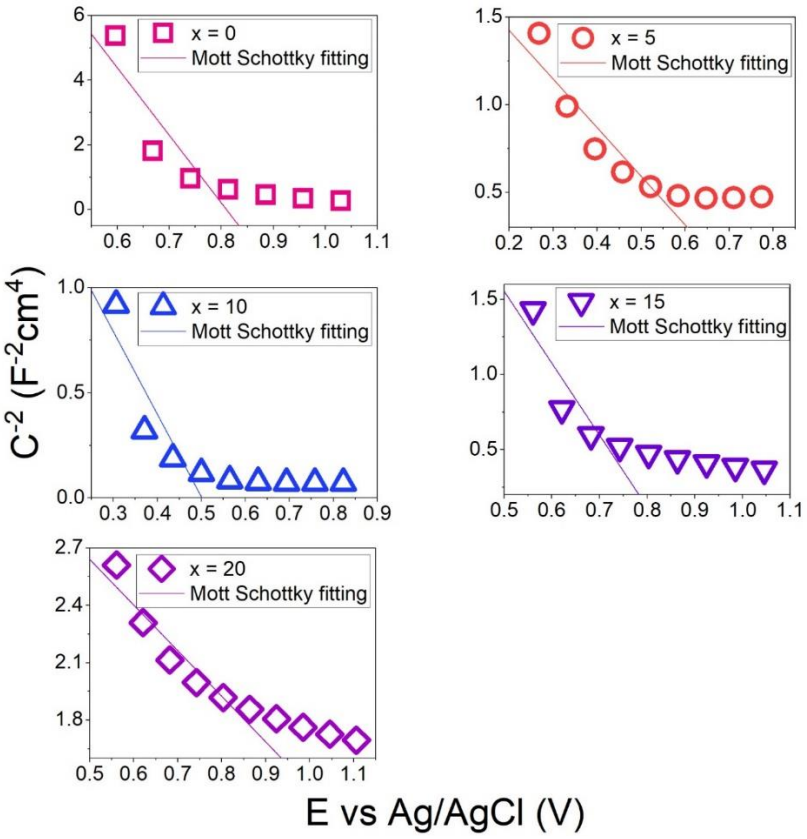

Figure 6.10 Mott Schottky fitting with pH variation suggesting n-type behavior in pH =1 and 14 while p-type behavior is observed in pH=7.

6.3.5 Stability Test

Fig.6.11(a) shows the chronopotentiometric stability of $n = 15$ DH-MIEC in environment-friendly neutral medium for more than 25 h. However, the sample n =10 and 20 degraded while chromopotentiometric stability.

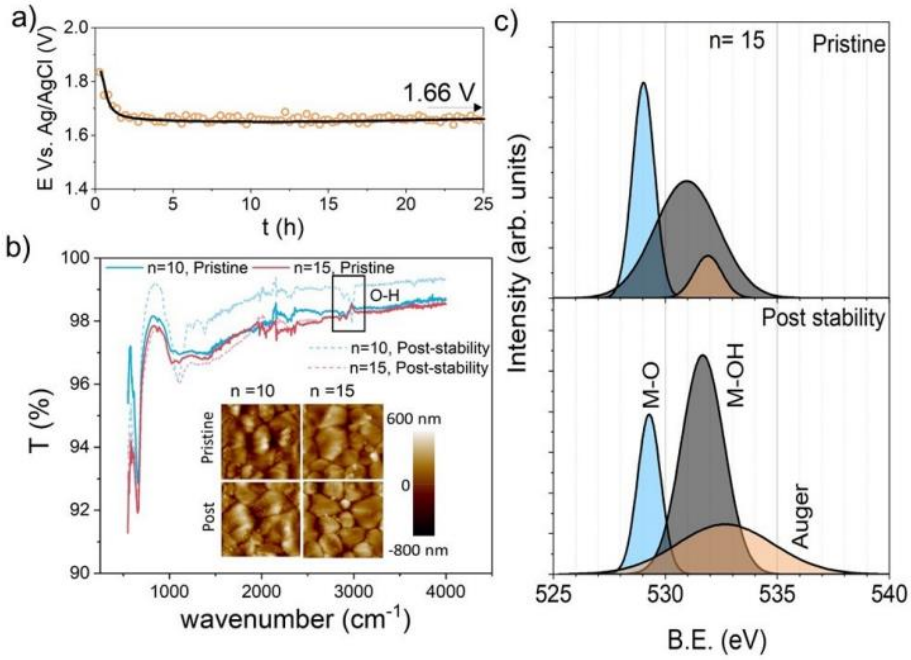

Figure 6.11 (a) Chronopotentiometric stability in OER regime for 25 h resulting in the potential of 1.66 V for $\boldsymbol{n} = 15$ **(b)** Variation of transmittance from IR spectra, inset shows the surface topographical images before and after stability test for $\boldsymbol{n} = 10$ and $\boldsymbol{n} = 15$ DH-MIECs **(c)** Deconvoluted O XPS spectra before and after stability test for $\boldsymbol{n} = 15$ DH-MIEC.

This has been confirmed through IR spectra for $n = 10$ DH-MIEC (Fig.6.11(b)) showing the formation of complex coordination compounds with -OH bond where the transmittance increases near 3000 cm^{-1}[211] Fig. 6.11(b) inset shows the topographical images for $n = 10$ from AFM indicating larger grain size along with adsorbed -OH post stability. While, for $n = 15$, grain size has not altered post stability.

Fig. 6.11(c) shows the deconvoluted O-XPS spectra for $n = 15$ and can be seen that the intensities of M-O and M-OH peaks have increased along with the broadening of Auger peak post stability. This broadening in Auger peak is compensated with the red shift and decreased FWHM in M-OH peak post stability.

6.4 Conclusion

In this chapter, heterostructure LSFT/ZnO/LSFT is explored as a multifunctional catalyst for the simultaneous HER/OER/ORR in the neutral medium. XRD pattern shows the presence of orthorhombic phase Pbnm of LSFT and hexagonal phase (P63mc) of ZnO. A relative conductivity is four times higher for all four heterostructure in comparison to parent LSFT. Variation of I/I_o vs time shows the MIEC behavior of the heterostructure. The activation energy calculated from the Arrhenius equation gives 75 meV suggest the polaronic conduction in all DH-MIECs. XPS analysis shows that metal-O bond (Fe-O, Ti-O, Sr-O, La-O) is present in LSFT and $n = 15$ while metal-OH present in parent LSFT,10, and 15 DH-MIECs. Electrochemical characterization have been carried out in neutral medium Na_2SO_4 and significant change in OER/ORR and HER behavior observed in all DH-MIECs with parent LSFT. ORR increases with the thickness whereas HER and OER potential shifted to more positive potential and a significant increase in OER current observed. The log-log plot confirms the charge transfer via O-diffusion method as the slope is greater than 0.5 value. A lesser transient response observed in all the DH-MIECs which make them suitable for hole transport behavior. Mott Schottky analysis suggest p-type nature for all DH-MIECs including parent LSFT. Chronopotentiometry test shows the stability of the DH-MIECs in which only $n = 15$ was stable for 24 h in the applied voltage 2V, which is also confirmed through the post and pristine FTIR, AFM, and XPS characterization.